JACS
JOURNAL OF THE AMERICAN CHEMICAL SOCIETY
pubs.acs.org/JACS
Article

Lithium Metal-Compatible Antifluorite Electrolytes for Solid-State Batteries

Pengcheng Yu, Haochang Zhang, Fiaz Hussain, Jing Luo, Wen Tang, Jiuwei Lei, Lei Gao, Denys Butenko, Changhong Wang, Jinlong Zhu, Wen Yin, Hao Zhang, Songbai Han,* Ruqiang Zou,* Wei Chen, Yusheng Zhao, Wei Xia,* and Xueliang Sun*

Cite This: *J. Am. Chem. Soc.* 2024, 146, 12681−12690
Read Online

ABSTRACT: Lithium (Li) metal solid-state batteries feature high energy density and improved safety and thus are recognized as promising alternatives to traditional Li-ion batteries. In practice, using Li metal anodes remains challenging because of the lack of a superionic solid electrolyte that has good stability against reduction decomposition at the anode side. Here, we propose a new electrolyte design with an antistructure (compared to conventional inorganic structures) to achieve intrinsic thermodynamic stability with a Li metal anode. Li-rich antifluorite solid electrolytes are designed and synthesized, which give a high ionic conductivity of 2.1×10^{-4} S cm^{-1} at room temperature with three-dimensional fast Li-ion transport pathways and demonstrate high stability in Li−Li symmetric batteries. Reversible full cells with a Li metal anode and $LiCoO_2$ cathode are also presented, showing the potential of Li-rich antifluorites as Li metal-compatible solid electrolytes for high-energy-density solid-state batteries.

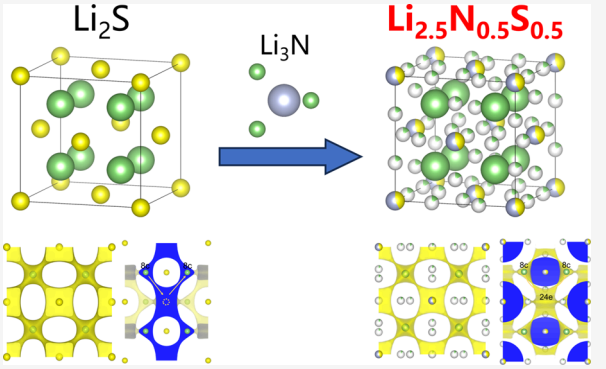

INTRODUCTION

The transition from fossil fuels to sustainable energy has created unprecedented demands for energy storage systems.[1,2] Lithium-ion batteries (LIBs), one of the most widely used energy storage systems, have reached a bottleneck in terms of safety and energy density.[1,3,4] Alternatively, solid-state batteries based on inorganic solid electrolytes (SEs) have been proposed because of the excellent safety and wide operating temperature range.[3−9] The new battery technology removes the flammable organic liquid electrolytes of LIBs and could unlock the use of a Li metal anode for improving safety and energy density, leading to an ideal candidate for electric vehicles.[1,4,5,7,10−12] The theoretical capacity of the Li metal anode is almost 10 times higher than that of conventional graphite anodes of LIBs. Nevertheless, the development of Li metal solid-state batteries has been hindered by the lack of high-performance SEs that simultaneously possess a high ionic conductivity and good stability with Li metal anodes.[5,13−16]

Significant progress has been achieved in Li-conducting inorganic SEs over the past few decades. Some fast ionic conductors, such as $Li_{10}GeP_2S_{12}$, $Li_{1.3}Al_{0.3}Ti_{1.7}(PO_4)_3$, Li_3YCl_6, and $LiTaOCl_4$, were successfully synthesized with exceptionally high ionic conductivities that are even comparable with that of liquid electrolytes.[13,14,17−19] However, most superionic SEs are not compatible with Li metal anodes. The underlying reason for this phenomenon is the existence of high-valence cations (e.g., Ge^{4+}, Ti^{4+}, and Ta^{5+}) that are susceptible to reduction by the Li metal.[14,17] Reduction decomposition occurs at the SE-Li interface and produces electronically conducting metals or alloys with ionic conducting compounds, also known as the mixed ionic-electronic conductor.[13,20,21] This will cause continuous growth of the interphase layers and eventually lead to high interfacial resistance and battery failure.[18,20] Protective interfaces can be introduced to separate the SE from the Li anode through chemical optimization of the SEs (e.g., F-doping or forming LiPON-type SE) or post-modification of the surface of the as-formed SE layer and Li metal anode,[8,22−25] but these strategies often slow down the overall ionic conduction or require sophisticated and time-consuming interfacial engineering technologies. Therefore, ideal SEs are anticipated to be thermodynamically stable with metallic Li, which, however, has rarely been achieved.

Considering that the high-valence cations are the origin of the instability of SEs against Li, here, we propose an antistructure design to eliminate the non-Li cations from the

Received: February 12, 2024
Revised: April 9, 2024
Accepted: April 10, 2024
Published: April 23, 2024

https://doi.org/10.1021/jacs.4c02170
J. Am. Chem. Soc. 2024, 146, 12681−12690

chemical composition of SEs to achieve intrinsic thermodynamic stability toward Li (Figure 1). Generally, the backbone

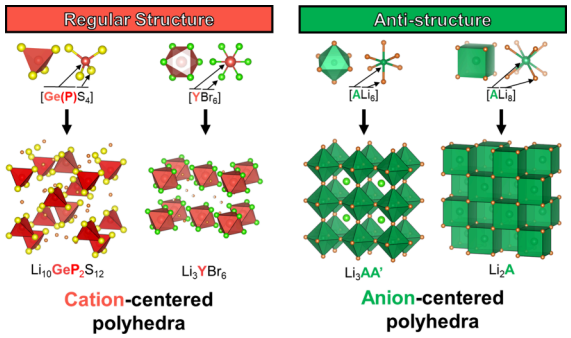

Figure 1. Design principles of antistructure materials.

of conventional SEs is constituted by high-valence cation-centered polyhedra with each cation coordinated by six or four anions (usually oxide, sulfide, and halide ions), for example, $(Ge/P)S_4$ tetrahedra and YBr_6 octahedra in the most representative $Li_{10}GeP_2S_{12}$ sulfide and Li_3YBr_6 halide SEs, respectively.[14,17,26] The high-valence cations (e.g., Ge/P and Y) are necessary for maintaining the structural stability of the SEs.[17,26,27] In contrast, the proposed antistructures have reversed ionic arrangement where anions occupy the center of polyhedra and cations are at the corners. This means that Li^+ ions can act as the only type of cation ligand in the anion-centered polyhedra of a Li-rich antistructure and, in the meantime, as the charge carriers for SEs. Therefore, intrinsic stability to metallic Li can be anticipated for the structure as all the atoms except Li are at the lowest valence state.[26−28] Following the design principle, we here successfully synthesized a Li-conducting antistructure, antifluorite $Li_{2+x}N_xS_{1-x}$ ($0 < x < 1$), based on a new Li−N−S chemistry. A high ionic conductivity at room temperature and extraordinary Li compatibility are achieved from the SEs. Moreover, an interesting interstitial Li configuration responsible for the fast Li transport in the antifluorite structure is first revealed by an in-depth structure analysis through neutron and synchrotron X-ray diffractions, motivating the development of new advanced SEs for Li metal solid-state batteries.

RESULTS AND DISCUSSION

The design of antifluorite $Li_{2+x}N_xS_{1-x}$ was inspired by the fluorite-type $Ba_{0.6}La_{0.4}F_{2.4}$ compound that exhibits the highest conductivity of fluoride ion (F^-) among all known fluorites.[29] The $Ba_{0.6}La_{0.4}F_{2.4}$ structure comprises a bivalent cation of Ba^{2+}, a trivalent cation of La^{3+}, and an anion of F^-.[29] The antifluorite-type structure is electrically reversed, with S^{2-}, N^{3-}, and Li^+ replacing the Ba^{2+}, La^{3+}, and F^- ions in the $Ba_{0.6}La_{0.4}F_{2.4}$ structure, respectively. This leads to analogues of "$S_xN_{1-x}Li_{2+x}$", which is notated as $Li_{2+x}N_xS_{1-x}$ ($0 < x < 1$) following the "cation-first" conventions.

As illustrated in Figure 2a and Figure S1, ternary phase diagrams are constructed based on the convex hull of the normalized energy per atom projected into the compositional coordinate space to check the phase stability of Li−N−S systems. The computed hull energy indicates that $Li_{2.5}N_{0.5}S_{0.5}$ is thermodynamically metastable with a hull energy of 17 meV/atom at 0 and 300 K, indicating that it can be synthesized by vibrational entropic configuration.

High-performance all-solid-state batteries require ultrafast ion conductors that are compatible with reductive metal anodes. To study the thermodynamic intrinsic electrochemical stability window (ESW) of $Li_{2.5}N_{0.5}S_{0.5}$, Li grand potential

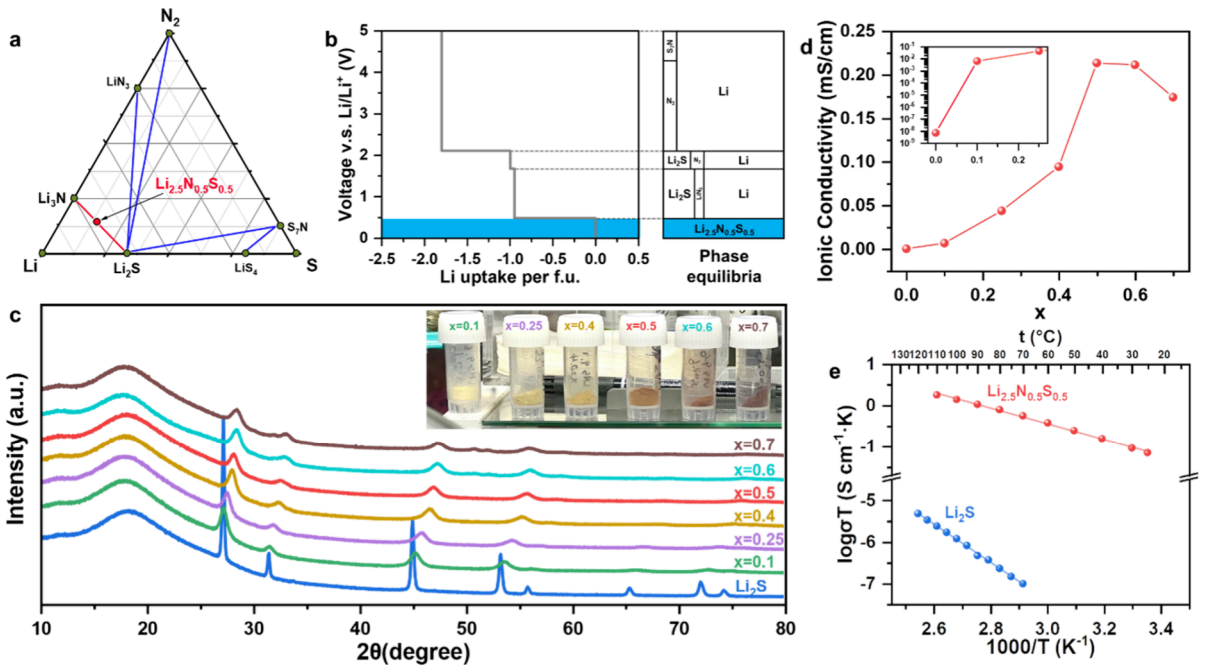

Figure 2. (a) Ternary phase diagram of the Li−N−S system at 0 K. The green dots represent stable phases. The red square represents the metastable phase $Li_{2.5}N_{0.5}S_{0.5}$ that can be decomposed into Li_2S and Li_3N. (b) Thermodynamic equilibrium voltage profile and phase equilibria for $Li_{2.5}N_{0.5}S_{0.5}$. The blue part indicates that $Li_{2.5}N_{0.5}S_{0.5}$ is stable with the Li metal anode against voltage vs Li^+/Li. (c) Powder X-ray diffraction (XRD) results and optical images of Li_2S and $Li_{2.5}N_{0.5}S_{0.5}$ (x = 0.1, 0.2, 0.25, 0.4, 0.5, 0.6, and 0.7). (d) Ionic conductivities of Li_2S and $Li_{2+x}N_xS_{1-x}$. (e) Arrhenius plots of Li_2S and $Li_{2.5}N_{0.5}S_{0.5}$.

https://doi.org/10.1021/jacs.4c02170
J. Am. Chem. Soc. 2024, 146, 12681−12690

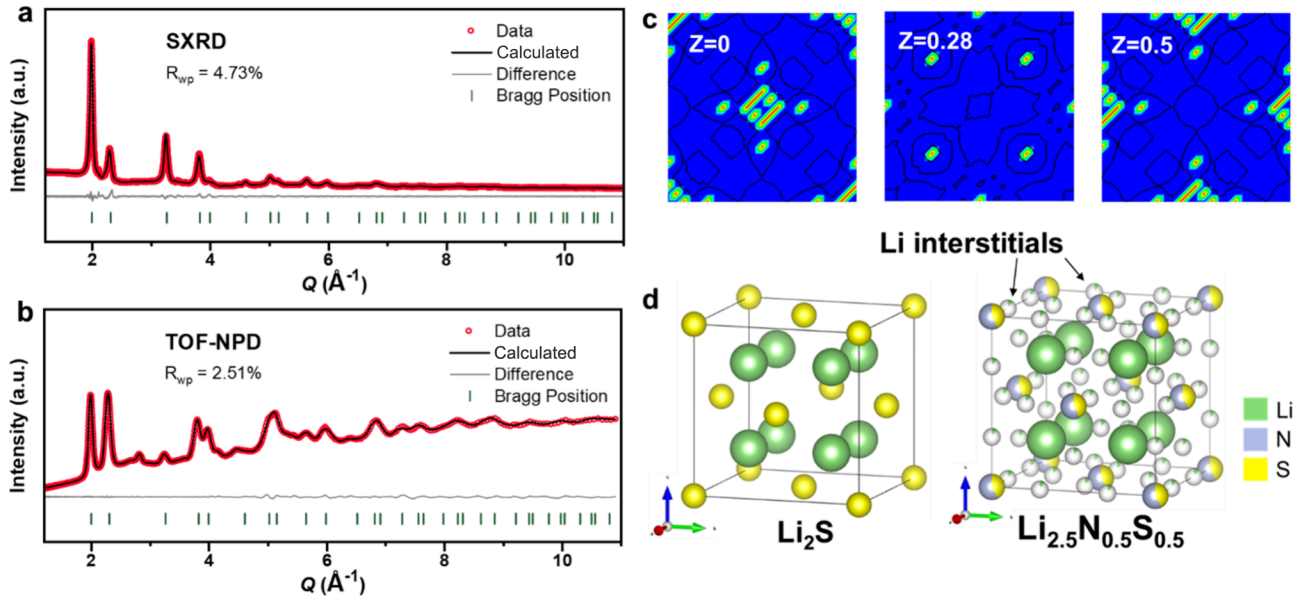

Figure 3. Joint refinement of synchrotron XRD and neutron diffraction results. (a) Synchrotron XRD plot and the refinement result. (b) Neutron diffraction plot and the refinement result. (c) Difference Fourier maps of $Li_{2.5}N_{0.5}S_{0.5}$ when z = 0, 0.28, and 0.5. (d) Schematics of the crystal structures of Li_2S and $Li_{2.5}N_{0.5}S_{0.5}$.

phase diagrams under different Li potentials were constructed based on the study of the average voltage embedded in the high Li potential:

$$\emptyset = E - \mu_{Li} N_{Li} \quad (1)$$

where E, μ_{Li}, and N_{Li} are the internal energy, Li chemical potential, and number of Li atoms in the system, respectively. The low voltage ($\mu_{Li} \approx \mu^0_{Li} - 5eV$) corresponds to the cathode interface, and the high voltage ($\mu_{Li} \approx \mu^0_{Li}$) corresponds to the anode interface. Here, μ^0_{Li} is the energy of metallic Li. It is clear from Figure 2b that $Li_{2.5}N_{0.5}S_{0.5}$ exhibits intrinsic stability with the Li metal anode.

A series of $Li_{2+x}N_xS_{1-x}$ ($0 < x < 1$) compounds was synthesized by ball-milling a mixture of Li_2S and Li_3N. The products are obtained at various starting material ratios with x = 0.1, 0.25, 0.4, 0.5, 0.6, and 0.7. The inset in Figure 2c shows the gradient colors of $Li_{2+x}N_xS_{1-x}$ samples, ranging from light yellow (x = 0.1) to orange (x = 0.5) and finally to purple (x = 0.7), which are distinct from the starting materials Li_2S (white) and Li_3N (dark red), indicating a decreasing optical bandgap with an increasing nitrogen content. Powder X-ray diffraction (PXRD) (Figure 2c) reveals a crystalline phase of the $Li_{2+x}N_xS_{1-x}$ samples similar to that of the Li_2S starting material (*Fm*-3*m*, ICSD 642291), indicating the formation of a solid solution. Notably, peak positions of $Li_{2+x}N_xS_{1-x}$ samples shift to higher diffraction angles with an increasing x value (i.e., nitrogen content), corresponding to the contraction of crystal unit cells. However, the shift in peak positions becomes less pronounced for values exceeding 0.5. This suggests that the nitrogen content within the antifluorite $Li_{2+x}N_xS_{1-x}$ structure has approached its tolerance limit.

The Li^+ transport property of $Li_{2+x}N_xS_{1-x}$ was first characterized by electrochemical impedance spectroscopy (EIS) at different temperatures. As shown in Figure S2, the Nyquist plots exhibit typical characteristics of solid-state superionic conductors, featuring a semicircle and a Warburg tail. The total ionic conductivity can be calculated by determining the total resistance from the intersection between the semicircle and the Warburg tail. Figure 2d shows the ionic conductivity of $Li_{2+x}N_xS_{1-x}$ solid electrolytes with varying starting material ratios from x = 0.1 to x = 0.7. The curve exhibits a volcano-like shape. More specifically, the ionic conductivity rapidly increases with the increase in x at relatively low nitrogen concentrations; $Li_{2.5}N_{0.5}S_{0.5}$ displayed the highest ionic conductivity of 2.1×10^{-4} S cm^{-1} at room temperature (RT, 27 °C), and a slight decrease in ionic conductivity was observed at higher x values (x = 0.6 and 0.7). This transition point is consistent with the solid solubility limit. It is worth noting that the ionic conductivity of $Li_{2.5}N_{0.5}S_{0.5}$ is 7 orders of magnitude higher than that of the Li_2S precursor ($\sim 10^{-11}$ S cm^{-1}), even though they have similar crystal structures as observed by PXRD (Figure 2c). Therefore, $Li_{2.5}N_{0.5}S_{0.5}$ was chosen as a representative solid electrolyte for ionic conductivity measurements in a wide temperature range from RT to 110 °C (Figure S3). The Arrhenius plot, compared to that of Li_2S, is shown in Figure 2e. The activation energy of $Li_{2.5}N_{0.5}S_{0.5}$ was calculated to be 0.35 eV based on the Arrhenius equation. The value is close to that of the most representative superionic conductor $Li_{10}GeP_2S_{12}$ (0.25 eV) and is significantly lower than that of Li_2S (0.85 eV), indicating fast ion conduction in the electrolyte.[17] In addition, the electronic conductivity of $Li_{2.5}N_{0.5}S_{0.5}$ was determined by the direct-current polarization method (Figure S4a). The fitted U–I curve reveals that the electronic conductivity of $Li_{2.5}N_{0.5}S_{0.5}$ is lower by 4 orders of magnitude compared to its ionic conductivity (Figure S4b).

The crystal structure of $Li_{2.5}N_{0.5}S_{0.5}$ is characterized using synchrotron X-ray diffraction (SXRD) and Rietveld refinement (Figure 3a). As designed, the disordered N and S atoms co-occupy the Wyckoff 4*a* sites in the antifluorite structure (*Fm*-3*m* space group). Due to the introduction of nitrogen atoms, $Li_{2.5}N_{0.5}S_{0.5}$ possesses a higher concentration of Li atoms in the lattice compared to Li_2S. However, the fully occupied 8*c* Li sites are insufficient to accommodate additional Li^+. This necessitates the search for precise positions of interstitial Li^+. However, due to the low scattering factor of Li atoms toward

https://doi.org/10.1021/jacs.4c02170
J. Am. Chem. Soc. 2024, 146, 12681−12690

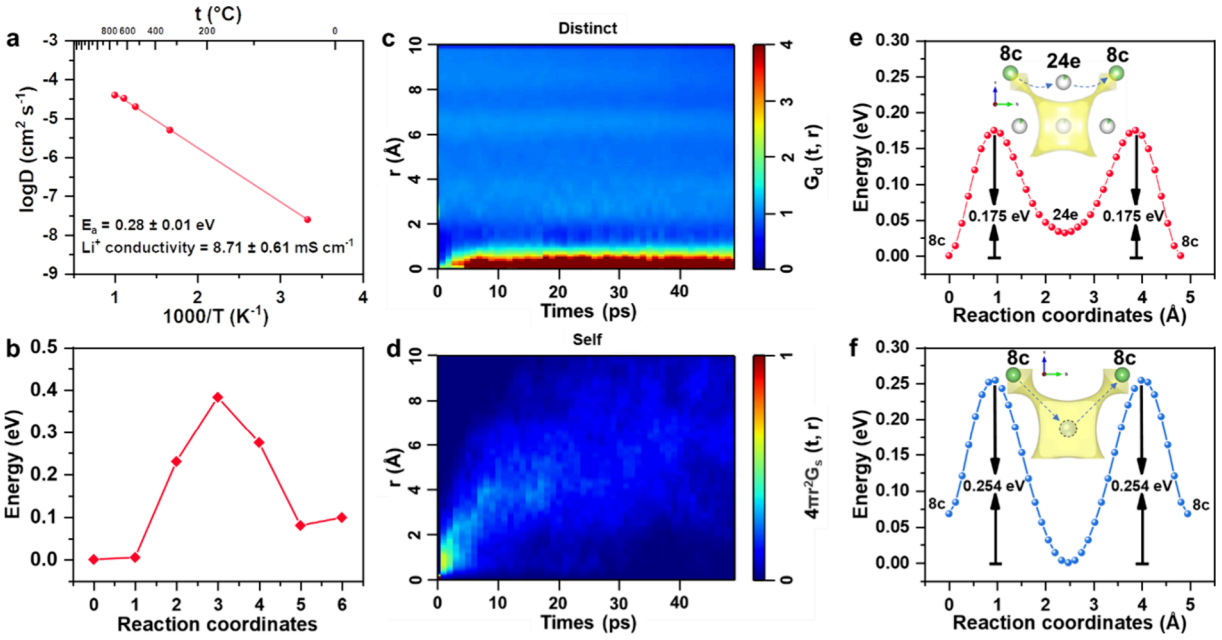

Figure 4. (a) Arrhenius plot for diffusivity with an extrapolated diffusion coefficient at 300 K. (b) Migration barrier of the Li atom for a selected path computed using NEB. (c) Distinct-part G_d and (d) self-part G_s of the van Hove correlation function for $Li_{2.5}N_{0.5}S_{0.5}$ at 900 K. Migration barrier of Li atoms in (e) $Li_{2.5}N_{0.5}S_{0.5}$ and (f) Li_2S and isosurface with an isovalue of 0.001 of Li probability density distribution extracted using BSVE.

X-rays, the determination of an accurate crystal structure and Li^+ migration pathways of $Li_{2.5}N_{0.5}S_{0.5}$ requires additional Li-sensitive characterization techniques.

Owing to the distinctive scattering properties of Li atoms with neutrons, time-of-flight neutron powder diffraction (TOF-NPD) is a powerful tool to determine the precise Li positions within the lattice. Initially, utilizing a crystal structure of $Li_{2.5}N_{0.5}S_{0.5}$ derived from the refinement results of SXRD in combination with TOF-NPD patterns (Figure 3b), a differential Fourier map (Figure S5) was generated. The results revealed pronounced positive signal distributions in the 001 planes at z = 0, 0.28, and 0.5 in the differential Fourier maps (Figure 3c), corresponding to the presence of interstitial Li sites (Wyckoff 24*e* site) at the octahedral voids in the lattice.

After the introduction of the 24*e* interstitial Li sites, joint Rietveld refinement analysis of the SXRD and TOF-NPD patterns was conducted. The structural parameters resulting from this analysis are provided in Table S1. The crystal structure of $Li_{2.5}N_{0.5}S_{0.5}$, as displayed in Figure 3d, affirms the successful realization of the anticipated antifluorite arrangement. The refinement result of SXRD patterns based on the space group of *Fm*-3*m* reveals that the lattice constant *a* of $Li_{2.5}N_{0.5}S_{0.5}$ was determined to be about 5.458 Å, which is smaller than that of the Li_2S precursor (Figure 3d). This can be understood by the smaller ionic radii of N^{3-} (132 pm) than that of S^{2-} (170 pm).[30] Most of the Li atoms occupy the regular 8*c* sites (Li1), and the excessive Li introduced by the substitution of N^{3-} for S^{2-} is accommodated at the 24*e* (Li2) interstitial sites. The occupancies of the Li sites were refined and found to be about 0.966 for Li2, while 8*c* sites were still found to be completely occupied, which is the same as the complete occupation in conventional fluorite and antifluorite structures (e.g., Li_2S has only one type of Li site, and it is completely occupied, as shown in Figure 3d). This means that the Li sites in antifluorite $Li_{2.5}N_{0.5}S_{0.5}$ are deficient with considerable vacancies to accommodate fast Li migration, which may explain the high ionic conductivity of $Li_{2.5}N_{0.5}S_{0.5}$. Moreover, even though doping or Li depletion can introduce Li vacancies in the nonionic-conductive perfect antiperovskite structure to promote ion conduction through neighboring ionic hopping,[26,27,31] the results are not as effective as that reported here in the antifluorite system.

Ab initio molecular dynamics (AIMD) simulation was further carried out using a canonical ensemble (NVT) to compute the diffusion coefficient and Li^+ conductivity for $Li_{2.5}N_{0.5}S_{0.5}$. Mean square displacement (MSD) and diffusion coefficients for $Li_{2+x}N_xS_{1-x}$ are extracted using the VASPkit code. The MSD curves extracted at each temperature are plotted in Figure S6, which shows very high MSD at each temperature and a linear increase during AIMD simulation time and results in a high computed Li ionic conductivity of 8.31×10^{-3} S cm^{-1} with an activation energy of 0.28 eV (Figure 4a). The variance between experimental values and AIMD-simulated values can be attributed to the sensitivity of the ionic conductivity to the diffusion coefficient. For example, $Li_7P_3S_{11}$ exhibits an experimental ionic conductivity in the range of 3.2×10^{-3} to 1.7×10^{-2} S cm^{-1},[32−34] whereas the theoretically predicted intrinsic Li ionic conductivity values are as high as 5.7×10^{-2} and 7.2×10^{-2} S cm^{-1}.[35,36] The van Hove correlation function (G) was used to understand the Li diffusion mechanism and correlation motion of Li ions based on a distinct part (G_d) and self-part (G_s) at 600−1000 K temperature during AIMD simulations (Figure S7). The G_d part in Figure 4c represents a peak at r < 1 Å at the start of the simulation time, which results in a very high correlation of Li diffusion in $Li_{2.5}N_{0.5}S_{0.5}$. Similarly, the peaks continue toward the large r values with the increase in simulation time t in the G_s part (Figure 4d), which implies high Li diffusion. The Li probability density function (PDF) is plotted in Figure S8 for $Li_{2.5}N_{0.5}S_{0.5}$ to understand the Li diffusion path, which indicates that $Li_{2.5}N_{0.5}S_{0.5}$ is a three-dimensional superionic conductor in which Li ions move equally in all directions. The

https://doi.org/10.1021/jacs.4c02170
J. Am. Chem. Soc. 2024, 146, 12681−12690

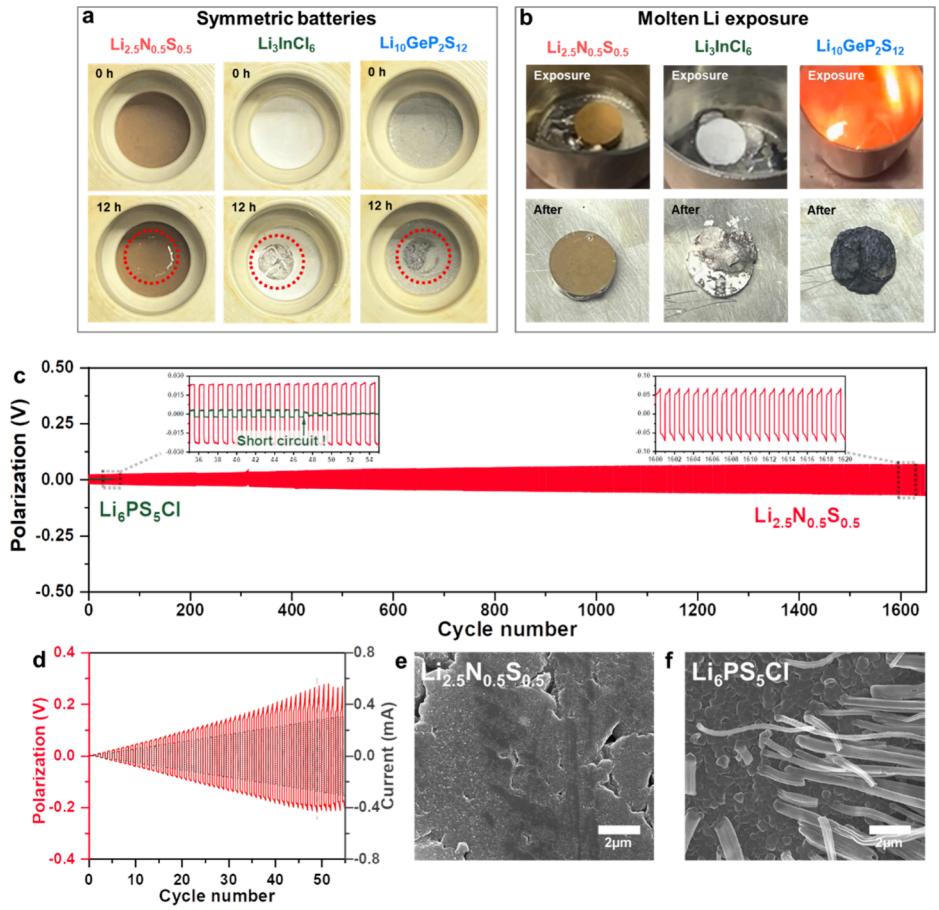

Figure 5. (a) Pictures of solid electrolytes before and after 12 h of aging in symmetric cells. (b) Pictures of solid electrolyte pellets being exposed to melt Li metal. (c) Schematic of symmetric batteries with Li_6PS_5Cl and $Li_{2.5}N_{0.5}S_{0.5}$ solid electrolytes. Zoomed figures correspond to 35−55 and 1600−1620 h after the cycles start. (d) Result of rate test of the symmetric battery with the $Li_{2.5}N_{0.5}S_{0.5}$ solid electrolyte. The red plot/axis corresponds to the overpotential of the symmetric battery, and the dark gray plot/axis corresponds to the charging/discharging current. (e, f) SEM picture of the surface of Li_6PS_5Cl (f) and $Li_{2.5}N_{0.5}S_{0.5}$ (e) pellets after 100 h cycles in symmetric batteries.

PDF result also confirms the three-dimensional diffusion of $Li_{2.5}N_{0.5}S_{0.5}$ obtained by MSD at each temperature (Figure S9). The antifluorite $Li_{2.5}N_{0.5}S_{0.5}$ solid electrolyte exhibits optimized three-dimensioal diffusion pathways for Li^+ migration and significantly improved Li^+ conductivity by introducing new interstitial lithium sites. To find the migration barrier energy for Li, a CI-NEB calculation was also carried out for $Li_{2.5}N_{0.5}S_{0.5}$. The result shows that the Li migration barrier is 0.38 eV (Figure 4b), which is in excellent agreement with the experimental activation energy result.

The bond valence site energy (BVSE) method was performed based on the structure of $Li_{2.5}N_{0.5}S_{0.5}$ to elucidate the mechanism of Li^+ migration. Detailed information on the calculations can be found in the Supporting Information. As depicted in Figure S10, the Li^+ diffusion channels are illustrated by using yellow isosurfaces to mark the Li^+ probability density obtained from BVSE simulations. BVSE analysis revealed that the introduction of interstitial 24*e* Li^+ sites in $Li_{2.5}N_{0.5}S_{0.5}$ provides a pathway of 8*c*-24*e*-8*c* for Li^+ hopping (Figure 4e and Figure S10d). The introduction of additional Li^+ cation sites in the $Li_{2.5}N_{0.5}S_{0.5}$ lattice also leads to a higher charge carrier concentration in addition to 3D Li^+ diffusion pathways, which results in higher Li^+ diffusion efficiency. The migration barrier of $Li_{2.5}N_{0.5}S_{0.5}$ was found to be 0.176 eV (Figure 4e). Comparatively, Li^+ can diffuse only through the 8c-interstitial site-8c pathway in the Li_2S lattice (Figure 4f and Figure S10f). The migration barrier of Li_2S is 0.254 eV. It is worth noting that the cell volume of Li_2S used in the BVS simulation is adopted from the ICSD database (a = 5.719 Å), while a smaller cell volume of Li_2S could result in a higher migration barrier in the calculations (e.g., 0.400 eV if a = 5.554 Å). The presence of superionic conduction in fluorite-type structures raised the expectation of high ionic conductivity in antifluorite-type structures, such as lithium sulfide; however, the Li^+ conductivity in such structures is notably low. This outcome suggests that the satisfactory Li^+ conductivity can be attributed to the unique anion disorder and cation defect chemistry in the $Li_{2.5}N_{0.5}S_{0.5}$ lattice.

Compared to best-performing solid electrolytes (such as $Li_{10}GeP_2S_{12}$ and $LiTaOCl_4$),[14,17,19,37] $Li_{2.5}N_{0.5}S_{0.5}$ demonstrates a significant advantage in Li metal anode compatibility with intrinsic thermodynamic stability (Figure 2b). The impedance of the Li metal symmetric cell with the $Li_{2.5}N_{0.5}S_{0.5}$ solid electrolyte was measured with an aging time from 5 min to 12 h to experimentally study the inherent compatibility of $Li_{2.5}N_{0.5}S_{0.5}$ with the Li metal. With the time increasing, the conductivity of the symmetric cell with $Li_{2.5}N_{0.5}S_{0.5}$ slightly decreased to 96.5% of the initial value (Figures S11a and S12), indicating a stable interface without chemical and electrochemical reactions between the Li anode and the solid electrolyte. In comparison, Li symmetric cells with Li_3InCl_6 demonstrate a significant drop in conductivity to

https://doi.org/10.1021/jacs.4c02170
J. Am. Chem. Soc. 2024, 146, 12681−12690

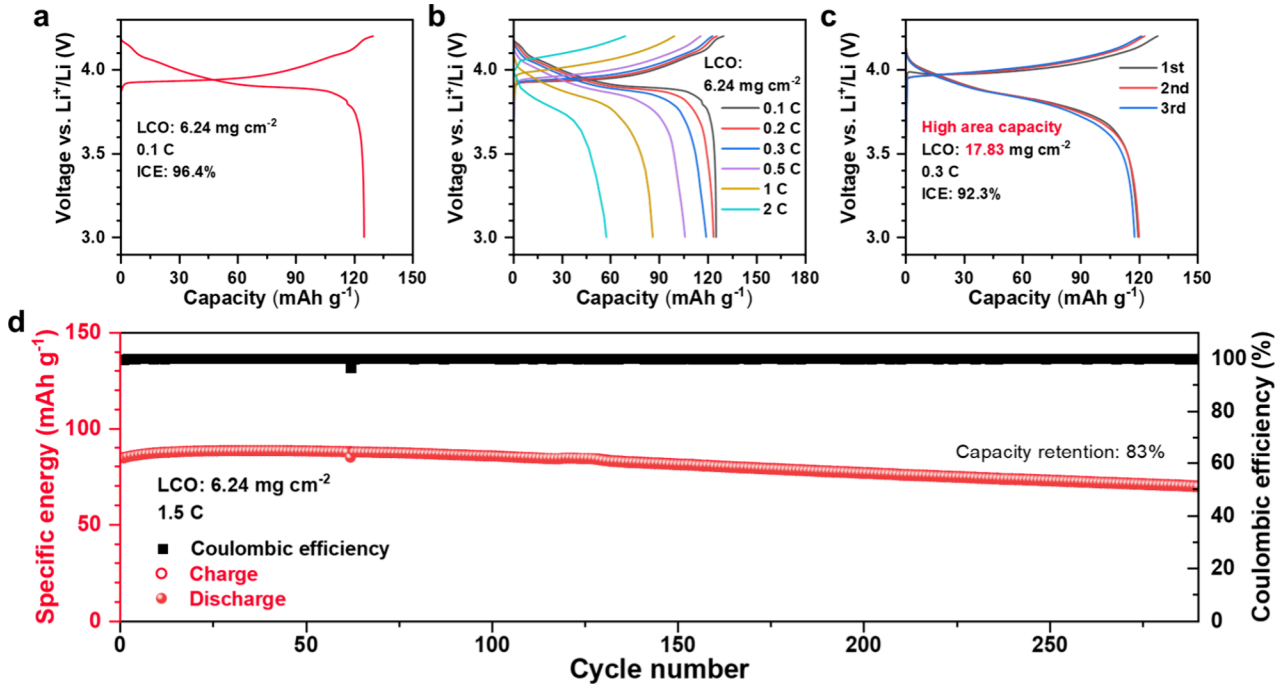

Figure 6. Electrochemical performance of the all-solid-state lithium metal batteries with the $Li_{2.5}N_{0.5}S_{0.5}$ solid electrolyte. (a) Charge/discharge curve at 0.1 C. (b) Charge/discharge curves at incremental cycling rates from 0.1 to 2 C. (c) Charge/discharge curves at 0.3 C of a high cathode loading of 17.83 mg cm^{-2} (2.5 mAh cm^{-2}). (d) Charge−discharge capacity and CE as a function of cycle number at 1.5 C. ICE, initial Coulombic efficiency.

8.94% of its initial value after 12 h (Figure S12); this is mirrored by the evident elevation of impedance as discerned from the EIS plots (Figure S11b). $Li_{10}GeP_2S_{12}$ symmetric cells show a similar impedance evolution to 7.60% of the initial value after aging (Figures S11c and S12). After resting for 12 h without applied voltage, all symmetric cells were disassembled, and the visual changes in the solid electrolyte pellets at the contact area with the Li metal anode were checked. As depicted in Figure 5a, no noticeable color variation was observed for the $Li_{2.5}N_{0.5}S_{0.5}$ solid electrolyte pellet and Li metal anode (Figure S13a) after 12 h of exposure. In contrast, the Li metal-contacted areas of the Li_3InCl_6 and $Li_{10}GeP_2S_{12}$ electrolyte pellets and the corresponding Li metal anodes (Figure S13b,c) exhibited darkened colors, implying potential electrolyte decompositions.

The possible interfacial component between $Li_{2.5}N_{0.5}S_{0.5}$ and the Li metal using the pseudobinary model was calculated, and it is shown in Figure S14. The reaction energy of $Li_{2.5}N_{0.5}S_{0.5}$ with the Li metal anode is zero, suggesting excellent interfacial stability between the anode and the solid electrolyte, whereas those of Li_3InCl_6 and $Li_{10}GeP_2S_{12}$ are large positive values. The stability calculation with other common anode materials was also presented for comparison (Figure S15 and Table S2).

The issue of thermal runaway in all-solid-state batteries and the strategy of achieving favorable anode−electrolyte contact through molten Li deposition are introducing novel dimensions to the investigation of solid electrolyte compatibility with the Li metal. To delve into the interfacial thermal stability of solid electrolytes with the Li metal, solid electrolyte pellets were placed atop molten Li in a nickel crucible on a hot stage at 280 °C. Images showing the evolution over molten Li exposure are presented in Figure 5b. After 1 min of exposure, no visible changes were observed on the $Li_{2.5}N_{0.5}S_{0.5}$ solid electrolyte pellet. The surface of the electrolyte pellet displayed no obvious alteration (except for some small Li droplets adhering to the pellet surface). This implies that the $Li_{2.5}N_{0.5}S_{0.5}$ solid electrolyte maintains robust thermal stability to the Li metal even at a high temperature. In contrast, the Li_3InCl_6 solid electrolyte pellet exhibited severe corrosion by molten Li, indicative of a reaction between the solid electrolyte and the Li metal. Surprisingly, the $Li_{10}GeP_2S_{12}$ solid electrolyte was ignited violently within a few seconds of exposure to molten Li, even in an argon-filled glovebox, and ultimately turned black.

Li metal symmetric cells with the $Li_{2.5}N_{0.5}S_{0.5}$ electrolyte were constructed to verify the electrochemical stability against the Li anode. Figure 5c shows the typical charging/discharging profiles of a Li|$Li_{2.5}N_{0.5}S_{0.5}$|Li cell at the current density of 0.1 mA cm^{-2}. The cell was cycled for over 1600 h. The Li metal symmetric cell was also tested at a higher current density of 0.7 mA cm^{-2}, demonstrating good reversibility (Figure S16). The uniform voltage curves indicated the efficient and stable transport of Li^+ ions. For comparison, the Li|Li_6PS_5Cl|Li cell showed a short circuit after only 50 cycles under the same condition. Scanning electron microscopy (SEM) was performed to further investigate the failure mechanism of the symmetric Li metal cells by observing the surface morphology of the solid electrolyte pellet after cycling. As shown in Figure 5e, no Li dendrites were observed on the surface of the $Li_{2.5}N_{0.5}S_{0.5}$ solid electrolyte after 50 cycles in the symmetric cell. In contrast, Figure 5f shows that thick worm-like dendrites have grown in the Li_6PS_5Cl solid electrolyte under identical cycling conditions. These results suggest uniform Li plating−stripping for $Li_{2.5}N_{0.5}S_{0.5}$-based cells. X-ray photoelectron spectroscopy (XPS) was employed to characterize the $Li_{2.5}N_{0.5}S_{0.5}$ solid electrolyte pellet after symmetric cell cycling, as depicted in Figure S17. Peaks derived from the fitting results of Li 1s, N 1s, and S 2p exhibit no discernible changes,

https://doi.org/10.1021/jacs.4c02170
J. Am. Chem. Soc. 2024, 146, 12681−12690

suggesting the good stability of $Li_{2.5}N_{0.5}S_{0.5}$ against the Li metal in the symmetric cell. The rate-performance test was further performed with the Li|$Li_{2.5}N_{0.5}S_{0.5}$|Li symmetric cell with a stepwise increase in current rates of 0.03 mA cm^{-2}. As shown in Figure 5d, $Li_{2.5}N_{0.5}S_{0.5}$ delivers a high critical current density of 1.41 mA cm^{-2}.

The excellent Li metal compatibility of the $Li_{2.5}N_{0.5}S_{0.5}$ solid electrolyte supports the use of Li metal as the anode in solid-state full batteries. As a demonstration, full cells utilizing a bare Li metal anode and $LiCoO_2$ (LCO) cathode were constructed with the $Li_{2.5}N_{0.5}S_{0.5}$ electrolyte. Figure 6a presents the voltage profiles of full cells with a capacity loading of 6.24 mg cm^{-2}, cycled at 0.1 C (where 1 C = 140 mA g^{-1}) between 3 and 4.3 V versus Li^+/Li at RT. The initial discharge capacity is 125.2 mAh g^{-1} with a high initial Coulombic efficiency of 96.4%. As shown in Figure 6b, the rate performance of the full cell was tested with cycling rates from 0.1 to 2 C and displayed smooth voltage profiles at each C rate. Full cells with a higher area capacity of 17.83 mg cm^{-2} (2.5 mAh cm^{-2}) were also assembled and tested. As shown in Figure 6c, the cell still delivered a high initial discharge capacity of 119.4 mAh g^{-1} and the initial CE is up to 92.3%. The cycling performance of full cells was also confirmed by long cycling at 1.5 C. As shown in Figure 6d, the full cell delivered a stable capacity retention of 83% after 290 cycles, which reveals the electrochemical stability of $Li_{2.5}N_{0.5}S_{0.5}$ toward the Li metal anode in full cells. Compared with conventional inorganic solid electrolytes that have been paired with Li alloys (e.g., Li−In), the antifluorite $Li_{2.5}N_{0.5}S_{0.5}$ solid electrolytes achieve solid-state lithium metal batteries without any further modification at the interface, which is beneficial for achieving high energy density and cell manufacturing.

CONCLUSIONS

In summary, we report a Li-rich superionic conductor with intrinsic thermodynamic stability with a Li metal anode under a special design of antifluorite structure. The antifluorite $Li_{2.5}N_{0.5}S_{0.5}$ solid electrolyte exhibits optimized pathways for Li^+ migration and significantly improves Li^+ conductivity by introducing new interstitial lithium sites. The study emphasizes excellent Li metal compatibility from both simulation and experimental perspectives. Reversible Li−Li symmetric batteries and full cells with the Li metal anode and $LiCoO_2$ cathode are also demonstrated utilizing the $Li_{2.5}N_{0.5}S_{0.5}$ electrolyte, showing the potential of lithium-rich antifluorites as Li-compatible solid electrolytes for high-energy-density solid-state lithium metal batteries.

Future work on the antifluorite solid electrolyte will investigate the explicit nature of Li^+ migration, in which both traditional lithium ion hopping models and percolation models can be considered. The mechanism of anion disorder and entropy-driving Li^+ diffusion also needs to be studied. The electrochemical reactions of the antifluorite solid electrolyte and its compatibility with high areal loading and fast charging in an all-solid-state battery also require further investigation. We anticipate that materials devoid of high-valent cations have the potential to pave a new path for high-performance lithium metal all-solid-state batteries.

METHODS

All material handlings were performed in an Ar-filled glovebox (MIKROUNA, H_2O < 0.01 ppm, O_2 < 0.01 ppm).

Synthesis of the $Li_{2+x}N_xS_{1-x}$ Materials. $Li_{2+x}N_xS_{1-x}$ (x = 0.1, 0.25, 0.4, 0.5, 0.6, and 0.7) were synthesized through solid-state mechanochemical reactions. Stoichiometric mixtures of Li_2S (99.9%, Alfa Aesar) and Li_3N (99.9%, Alfa Aesar) were weighed with a total mass of 3 g. The powder was ground with an agate pestle in an agate mortar for 30 min to get mixtures of start materials. These mixtures were transferred to an 80 mL ZrO_2 pot filled with 30 g of ZrO_2 balls (5 and 10 mm diameters) and ball-milled with the Fritsch Pulverisette 7 at 500 rpm for 7.5 h. Ball milling lasted for 30 cycles, including 15 min of milling and 5 min of cooling. The mass ratio between the mixture and the ZrO_2 ball was 1:20.

X-ray Diffraction. The phase purity of the synthesized samples was checked by powder X-ray diffraction (PXRD). The air-sensitive solid electrolyte samples were ground in an agate mortar. Then, the powder samples were transferred to quartz glass sample holders and covered with a polyimide film (Kapton) to protect the sample from air exposure. The PXRD patterns were collected in the 2θ range from 10° to 80° (0.01° per step) using a diffractometer (PANalytical Emp3 Diffraction System) with Cu K_α radiation (λ = 1.5405 Å) at 45 kV and 40 mA. Samples for synchrotron X-ray diffraction (SXRD) were finely ground and transferred to 0.7 mm-diameter quartz glass capillaries and sealed with UV-curable adhesive. Room-temperature SXRD was performed at the Australian Synchrotron (λ = 0.69511 Å); 2θ was from 10° to 80° (0.002° per step).

Neutron Diffraction. Room-temperature time-of-flight neutron powder diffraction (TOF-NPD) was performed on a Multi-Physics Instrument (MPI) at China Spallation Neutron Source. The joint Rietveld refinement between the SXRD data and the multibank TOF-NPD data was performed with the GSASII software package,[38,39] using a full Voigt peak shape for SXRD patterns and pseudo-Voigt peak shape for TOF-NPD patterns. Except lattice parameters, weight percentage, atomic positions, fractions, and displacement parameters (U_{iso}) of the $Li_{2.5}N_{0.5}S_{0.5}$ phase and Li_3N impurity phase were jointly refined for SXRD and TOF-NPD patterns. Since the Li atom has a negative neutron scattering length, difference Fourier mapping was used to locate the Li positions. The Vesta software package was utilized for the visualization of crystal structures.[40]

Ionic Conductivity and Activation Energy Measurements. Powder samples were cold-pressed with a pressure of 4 tons (500 MPa) in customized Swagelok batteries with a plastic cylinder (10 mm diameter) and stainless-steel plugs for 5 min, obtaining pellets of approximately 10 mm in diameter and 1 mm in height. Electrochemical impedance spectroscopy (EIS) measurements were performed with the Biologic SP-300 instrument at the frequency range from 1 Hz to 1 MHz with 10 mV amplitude.

To gain Arrhenius plots, variable-temperature EIS was measured. The Swagelok battery was set in a variable temperature oven (Guangzhou Wusuo Environment Instrument, HSL/G-04), and the temperature increased from room temperature to 110 °C. Every temperature will hold for 2 h before collecting data to ensure that the thermal equilibrium is reached. The Li^+ diffusion activation energy E_a is determined by the following Arrhenius equation:

$$\sigma T = A\exp(-E_a/k_B T)$$

σ is the tested ionic conductivity, T is the Kelvin temperature, and k_B is the Boltzmann constant.

The electronic conductivity of the $Li_{2.5}N_{0.5}S_{0.5}$ solid electrolyte was measured by a direct current (DC) polarization test with the Autolab PGSTAT 302F at room temperature. The bias voltage ranged from 0.10 to 0.25 V.

Electrochemical Measurements. For the fabrication of Lilsolid electrolyteLi symmetric cells, $Li_{2.5}N_{0.5}S_{0.5}$ and Li_6PS_5Cl (99%, Kejing) were cold-pressed in the Swagelok battery with a pressure of 4 tons for 5 min. Li foils (99.9%, China Energy Lithium Co., Ltd., Φ6 mm, thickness of 100 μm) were attached to both sides of the solid electrolyte pellet. The cell was then subjected to constant uniaxial pressures of 0.1 ton (12.5 MPa) in two stainless-steel flanges connected by bolts. Galvanostatic cycling of the symmetric cell with $Li_{2.5}N_{0.5}S_{0.5}$ and Li_6PS_5Cl solid electrolytes was carried out with a LAND CT 2001A battery test system.

https://doi.org/10.1021/jacs.4c02170
J. Am. Chem. Soc. 2024, 146, 12681−12690

For full cell fabrication, the composite cathode consisted of $LiCoO_2$ powder (99.9%, Kelude) and $Li_{1.5}ZrCl_{4.75}O_{0.5}$ (synthesized by the ball milling method),[41] which were mixed in 70:30 (wt %) ratio for 30 min using an agate pestle and mortar. The fabrication of the full cells has the following procedures: 40 mg of Li_6PS_5Cl and 50 mg of Li_2ZrCl_4O were added into the Swagelok battery and pressed under 2 tons (250 MPa) for 2 min, 15 mg of $Li_{2.5}N_{0.5}S_{0.5}$ solid electrolyte powder was added to the anode side of the cylinder and pressed under 2 tons for 2 min, 7 mg of composite cathode material was added to the cathode side of the electrolyte layer and pressed under 4 tons for 5 min, Li foil (Φ6 mm, thickness of 100 μm) was attached to another side of the electrolyte layer, and the cell with flanges was pressed under the stacking pressure of 0.25 tons (31.25 MPa). Galvanostatic charge−discharge was performed on a LAND CT 2001A battery test system.

Li/Solid Electrolyte Chemical Reactions. To attach melted Li to $Li_{2.5}N_{0.5}S_{0.5}$, Li_3InCl_6 (99%, Kejing), and $Li_{10}GeP_2S_{12}$ (99%, Kejing), the Li metal was melted in a nickel crucible on a hot stage at 280 °C. Then, cold-pressed (uniaxial cold press of 4 tons for 5 min) solid electrolyte pellets were placed on the melted Li. The conditions for Lilsolid electrolyte|Li symmetric cells with $Li_{2.5}N_{0.5}S_{0.5}$, Li_3InCl_6, and $Li_{10}GeP_2S_{12}$ were the same as cells for galvanostatic cycling.

Microscopy and XPS. The morphology of samples was measured by HITACHI SU8010 field-emission scanning electron microscopy (FESEM). XPS was measured by an ULVAC-PHI PHI 5000 Versaprobe III. Transfer suitcases were used to isolate the sample from air exposure in a sample injection in FESEM and XPS.

Computational Method. First-principles DFT calculations were performed using the generalized gradient approximation (GGA)[42] with the Vienna Ab initio Simulation Package (VASP).[43,44] Electronic structure and total energy calculations were performed with an energy cutoff of 520 eV for plane waves and the k-point 7 × 7 × 7 with the Monkhorst−Pack scattering method.[45] The force and energy were converged to values within 10^{-2} eV/Å and 10^{-6} eV, respectively. The projector augmented wave (PAW) method[46] was used for core−valence interactions. The density of states (DOS) was calculated by the Heyd−Scuseria−Erznerhof (HSE06) functional.[47] Climbing image nudged elastic band (CI-NEB)[48] calculations were also performed to obtain Li-ion migration barrier energy based on static local-minimum structures. Spin-polarized calculations using the GGA + U method were performed for the relaxation of volume and atomic position in constructing a ternary phase diagram of the Li−N−S system at 0 K. Ab initio molecular dynamic (AIMD) simulations were used with a time step of 2 fs in the canonical (NVT) ensemble for 50 ps for which a 2 × 2 × 2 supercell model for $Li_{2.5}N_{0.5}S_{0.5}$ was used in simulation with a 1 × 1 × 1 k-point grid and a 400 eV energy cutoff in the temperature range of 600−1200 K. A detailed computational method for AIMD and electrochemical window voltage can be seen elsewhere.[49−51]

■ ASSOCIATED CONTENT

Data Availability Statement

The data used in this study are available from the authors upon reasonable request.

Supporting Information

The Supporting Information is available free of charge at https://pubs.acs.org/doi/10.1021/jacs.4c02170.

Diffraction data, results from first-principles calculations, electrochemical impedance data, electrochemical test results, Li metal anode photographs, and XPS results (PDF)

■ AUTHOR INFORMATION

Corresponding Authors

Songbai Han − *Academy for Advanced Interdisciplinary Studies, Southern University of Science and Technology, Shenzhen, Guangdong 518055, China;* orcid.org/0000-0002-7552-5317; Email: hansb@sustech.edu.cn

Ruqiang Zou − *School of Materials Science and Engineering, Peking University, Beijing 100871, China;* orcid.org/0000-0003-0456-4615; Email: rzou@pku.edu.cn

Wei Xia − *Eastern Institute for Advanced Study, Eastern Institute of Technology, Ningbo, Zhejiang 315201, China;* orcid.org/0000-0003-3164-2789; Email: wxia@eitech.edu.cn

Xueliang Sun − *Eastern Institute for Advanced Study, Eastern Institute of Technology, Ningbo, Zhejiang 315201, China; Department of Mechanical and Materials Engineering, University of Western Ontario, London, Ontario N6A 5B9, Canada;* orcid.org/0000-0003-0374-1245; Email: xsun9@uwo.ca

Authors

Pengcheng Yu − *Eastern Institute for Advanced Study, Eastern Institute of Technology, Ningbo, Zhejiang 315201, China; Department of Physics, Southern University of Science and Technology, Shenzhen, Guangdong 518055, China; Faculty of Science, National University of Singapore, Singapore 117546, Singapore*

Haochang Zhang − *Academy for Advanced Interdisciplinary Studies, Southern University of Science and Technology, Shenzhen, Guangdong 518055, China*

Fiaz Hussain − *Eastern Institute for Advanced Study, Eastern Institute of Technology, Ningbo, Zhejiang 315201, China;* orcid.org/0000-0002-2247-2063

Jing Luo − *Department of Mechanical and Materials Engineering, University of Western Ontario, London, Ontario N6A 5B9, Canada*

Wen Tang − *Eastern Institute for Advanced Study, Eastern Institute of Technology, Ningbo, Zhejiang 315201, China*

Jiuwei Lei − *Department of Physics, Southern University of Science and Technology, Shenzhen, Guangdong 518055, China*

Lei Gao − *School of Materials Science and Engineering, Peking University, Beijing 100871, China; Academy for Advanced Interdisciplinary Studies, Southern University of Science and Technology, Shenzhen, Guangdong 518055, China*

Denys Butenko − *Department of Physics, Southern University of Science and Technology, Shenzhen, Guangdong 518055, China;* orcid.org/0009-0007-7217-6274

Changhong Wang − *Eastern Institute for Advanced Study, Eastern Institute of Technology, Ningbo, Zhejiang 315201, China;* orcid.org/0000-0002-4201-0130

Jinlong Zhu − *Department of Physics, Southern University of Science and Technology, Shenzhen, Guangdong 518055, China;* orcid.org/0000-0002-7314-8394

Wen Yin − *Institute of High Energy Physics, Chinese Academy of Sciences (CAS), Beijing 100049, China*

Hao Zhang − *School of Metallurgical and Ecological Engineering, University of Science and Technology Beijing, Beijing 100083, China*

Wei Chen − *Faculty of Science, National University of Singapore, Singapore 117546, Singapore*

Yusheng Zhao − *Eastern Institute for Advanced Study, Eastern Institute of Technology, Ningbo, Zhejiang 315201, China*

Complete contact information is available at: https://pubs.acs.org/10.1021/jacs.4c02170

Author Contributions

The manuscript was written through contributions of all authors. All authors have given approval to the final version of the manuscript.

Notes

The authors declare no competing financial interest.

■ ACKNOWLEDGMENTS

This work was supported by the Zhejiang Provincial Natural Science Foundation of China under grant no. LY23B030003, the Natural Science Foundation of Ningbo under grant no. 2023J200, the National Natural Science Foundation of China under grant no. 12275119, and Singapore Ministry of Education under its AcRF Tier 2 grant no. MOE-T2EP10123-0001. The work was also supported by the Laboratory of Electrochemical Energy Storage Technologies, Academy for Advanced Interdisciplinary Studies (SUSTech), the Major Science and Technology Infrastructure Project of Material Genome Big-science Facilities Platform supported by the Municipal Development and Reform Commission of Shenzhen, and Center for Computational Science and Engineering at the Southern University of Science and Technology.

■ REFERENCES

(1) Kim, T.; Song, W.; Son, D.-Y.; Ono, L. K.; Qi, Y. Lithium-ion batteries: outlook on present, future, and hybridized technologies. *Journal of materials chemistry A* **2019**, *7* (7), 2942−2964.
(2) Li, M.; Lu, J.; Chen, Z.; Amine, K. 30 years of lithium-ion batteries. *Adv. Mater.* **2018**, *30* (33), 1800561.
(3) Famprikis, T.; Canepa, P.; Dawson, J. A.; Islam, M. S.; Masquelier, C. Fundamentals of inorganic solid-state electrolytes for batteries. *Nature materials* **2019**, *18* (12), 1278−1291.
(4) Xia, S.; Wu, X.; Zhang, Z.; Cui, Y.; Liu, W. Practical challenges and future perspectives of all-solid-state lithium-metal batteries. *Chem.* **2019**, *5* (4), 753−785.
(5) Wang, Q.; Jiang, L.; Yu, Y.; Sun, J. Progress of enhancing the safety of lithium ion battery from the electrolyte aspect. *Nano Energy* **2019**, *55*, 93−114.
(6) Zhang, S. S. Liquid electrolyte lithium/sulfur battery: Fundamental chemistry, problems, and solutions. *J. Power Sources* **2013**, *231*, 153−162.
(7) Lin, D.; Liu, Y.; Cui, Y. Reviving the lithium metal anode for high-energy batteries. *Nature Nanotechnol.* **2017**, *12* (3), 194−206.
(8) Chen, Y.; Li, W.; Sun, C.; Jin, J.; Wang, Q.; Chen, X.; Zha, W.; Wen, Z. Sustained Release-Driven Formation of Ultrastable SEI between Li6PS5Cl and Lithium Anode for Sulfide-Based Solid-State Batteries. *Adv. Energy Mater.* **2021**, *11* (4), 2002545.
(9) Morino, Y. Impact of surface coating on the low temperature performance of a sulfide-based all-solid-state battery cathode. *Electrochemistry* **2022**, *90* (2), 027001−027001.
(10) Fu, K.; Gong, Y.; Liu, B.; Zhu, Y.; Xu, S.; Yao, Y.; Luo, W.; Wang, C.; Lacey, S. D.; Dai, J.; Chen, Y.; Mo, Y.; Wachsman, E.; Hu, L. Toward garnet electrolyte−based Li metal batteries: An ultrathin, highly effective, artificial solid-state electrolyte/metallic Li interface. *Sci. Adv.* **2017**, *3* (4), No. e1601659.
(11) Manthiram, A.; Yu, X.; Wang, S. Lithium battery chemistries enabled by solid-state electrolytes. *Nat. Rev. Mater.* **2017**, *2* (4), 1−16.
(12) Wang, Q.; Wu, J.-F.; Lu, Z.; Ciucci, F.; Pang, W. K.; Guo, X. A New Lithium-Ion Conductor LiTaSiO5: Theoretical Prediction, Materials Synthesis, and Ionic Conductivity. *Adv. Funct. Mater.* **2019**, *29* (37), 1904232.
(13) Richards, W. D.; Miara, L. J.; Wang, Y.; Kim, J. C.; Ceder, G. Interface stability in solid-state batteries. *Chem. Mater.* **2016**, *28* (1), 266−273.
(14) Han, F.; Zhu, Y.; He, X.; Mo, Y.; Wang, C. Electrochemical stability of Li10GeP2S12 and Li7La3Zr2O12 solid electrolytes. *Adv. Energy Mater.* **2016**, *6* (8), 1501590.
(15) Zhou, L.; Minafra, N.; Zeier, W. G.; Nazar, L. F. Innovative approaches to Li-argyrodite solid electrolytes for all-solid-state lithium batteries. *Acc. Chem. Res.* **2021**, *54* (12), 2717−2728.
(16) Lee, Y.; Jeong, J.; Lee, H. J.; Kim, M.; Han, D.; Kim, H.; Yuk, J. M.; Nam, K. W.; Chung, K. Y.; Jung, H. G.; Yu, S. Lithium argyrodite sulfide electrolytes with high ionic conductivity and air stability for all-solid-state li-ion batteries. *ACS Energy Lett.* **2021**, *7* (1), 171−179.
(17) Kato, Y.; Hori, S.; Kanno, R. Li10GeP2S12-type superionic conductors: synthesis, structure, and ionic transportation. *Adv. Energy Mater.* **2020**, *10* (42), 2002153.
(18) Xu, R.; Wu, Z.; Zhang, S.; Wang, X.; Xia, Y.; Xia, X.; Huang, X.; Tu, J. Construction of all-solid-state batteries based on a sulfur-graphene composite and Li9. 54Si1. 74P1. 44S11. 7Cl0. 3 solid electrolyte. *Chem.− Eur. J.* **2017**, *23* (56), 13950−13956.
(19) Tanaka, Y.; Ueno, K.; Mizuno, K.; Takeuchi, K.; Asano, T.; Sakai, A. New Oxyhalide Solid Electrolytes with High Lithium Ionic Conductivity > 10 mS cm−1 for All-Solid-State Batteries. *Angew. Chem., Int. Ed.* **2023**, *62* (13), No. e202217581.
(20) Hu, H.; Liu, M. Interfacial studies of solid-state cells based on electrolytes of mixed ionic−electronic conductors. *Solid State Ionics* **1998**, *109* (3−4), 259−272.
(21) Lau, J.; DeBlock, R. H.; Butts, D. M.; Ashby, D. S.; Choi, C. S.; Dunn, B. S. Sulfide solid electrolytes for lithium battery applications. *Adv. Energy Mater.* **2018**, *8* (27), 1800933.
(22) Luo, J.; Sun, Q.; Liang, J.; Adair, K.; Zhao, F.; Deng, S.; Zhao, Y.; Li, R.; Huang, H.; Yang, R.; Zhao, S.; Wang, J.; Sun, X. Rapidly In Situ Cross-Linked Poly(butylene oxide) Electrolyte Interface Enabling Halide-Based All-Solid-State Lithium Metal Batteries. *ACS Energy Letters* **2023**, *8* (9), 3676−3684.
(23) Chen, Y.; Yao, L.; Chen, X.; Jin, J.; Wu, M.; Wang, Q.; Zha, W.; Wen, Z. Double-Faced Bond Coupling to Induce an Ultrastable Lithium/Li6PS5Cl Interface for High-Performance All-Solid-State Batteries. *ACS Appl. Mater. Interfaces* **2022**, *14* (9), 11950−11961.
(24) Li, Z.; Yu, R.; Weng, S.; Zhang, Q.; Wang, X.; Guo, X. Tailoring polymer electrolyte ionic conductivity for production of low-temperature operating quasi-all-solid-state lithium metal batteries. *Nat. Commun.* **2023**, *14* (1), 482.
(25) Zhou, X.; Li, Z.; Li, W.; Li, X.; Fu, J.; Wei, L.; Yang, H.; Guo, X. Regulating Na-ion Solvation in Quasi-Solid Electrolyte to Stabilize Na Metal Anode. *Adv. Funct. Mater.* **2023**, *33* (11), 2212866.
(26) Xia, W.; Zhao, Y.; Zhao, F.; Adair, K.; Zhao, R.; Li, S.; Zou, R.; Zhao, Y.; Sun, X. Antiperovskite electrolytes for solid-state batteries. *Chem. Rev.* **2022**, *122* (3), 3763−3819.
(27) Zhao, Y.; Daemen, L. L. Superionic conductivity in lithium-rich anti-perovskites. *J. Am. Chem. Soc.* **2012**, *134* (36), 15042−15047.
(28) Li, Y.; Zhou, W.; Xin, S.; Li, S.; Zhu, J.; Lü, X.; Cui, Z.; Jia, Q.; Zhou, J.; Zhao, Y.; Goodenough, J. B. Fluorine-doped antiperovskite electrolyte for all-solid-state lithium-ion batteries. *Angew. Chem., Int. Ed.* **2016**, *55* (34), 9965−9968.
(29) Mori, K.; Mineshige, A.; Saito, T.; Sugiura, M.; Ishikawa, Y.; Fujisaki, F.; Namba, K.; Kamiyama, T.; Otomo, T.; Abe, T.; Fukunaga, T. Experimental visualization of interstitialcy diffusion pathways in fast-fluoride-ion-conducting solid electrolyte Ba0. 6La0. 4F2. 4. *ACS Appl. Energy Mater.* **2020**, *3* (3), 2873−2880.
(30) Rahm, M.; Hoffmann, R.; Ashcroft, N. W. Atomic and ionic radii of elements 1−96. *Chem.− Eur. J.* **2016**, *22* (41), 14625−14632.
(31) Zhang, Y.; Zhao, Y.; Chen, C. Ab initio study of the stabilities of and mechanism of superionic transport in lithium-rich antiperovskites. *Phys. Rev. B* **2013**, *87* (13), No. 134303.
(32) Mizuno, F.; Hayashi, A.; Tadanaga, K.; Tatsumisago, M. High Lithium Ion Conducting Glass-Ceramics in the System $Li_2S-P_2S_5$. *Solid State Ionics* **2006**, *177* (26−32), 2721−2725.
(33) Hayashi, A.; Minami, K.; Mizuno, F.; Tatsumisago, M. Formation of Li^+ superionic crystals from the $Li_2S-P_2S_5$ melt-quenched glasses. *J. Mater. Sci.* **2008**, *43*, 1885−1889.

https://doi.org/10.1021/jacs.4c02170
J. Am. Chem. Soc. 2024, 146, 12681−12690

(34) Seino, Y.; Ota, T.; Takada, K.; Hayashi, A.; Tatsumisago, M. A sulphide lithium super ion conductor is superior to liquid ion conductors for use in rechargeable batteries. *Energy Environ. Sci.* **2014**, *7* (2), 627−631.
(35) Chu, I.-H.; Nguyen, H.; Hy, S.; Lin, Y.-C.; Wang, Z.; Xu, Z.; Deng, Z.; Meng, Y. S.; Ong, S. P. Insights into the Performance Limits of the $Li_7P_3S_{11}$ Superionic Conductor: A Combined First-Principles and Experimental Study. *ACS Appl. Mater. Interfaces* **2016**, *8* (12), 7843−7853.
(36) Chang, D.; Oh, K.; Kim, S. J.; Kang, K. Super-Ionic Conduction in Solid-State $Li_7P_3S_{11}$-Type Sulfide Electrolytes. *Chem. Mater.* **2018**, *30* (24), 8764−8770.
(37) Mo, Y.; Ong, S. P.; Ceder, G. First Principles Study of the $Li_{10}GeP_2S_{12}$ Lithium Super Ionic Conductor Material. *Chem. Mater.* **2012**, *24* (1), 15−17.
(38) Toby, B. H.; Von Dreele, R. B. GSAS-II: the genesis of a modern open-source all purpose crystallography software package. *J. Appl. Crystallogr.* **2013**, *46* (2), 544−549.
(39) Rietveld, H. M. A profile refinement method for nuclear and magnetic structures. *Journal of applied Crystallography* **1969**, *2* (2), 65−71.
(40) Momma, K.; Izumi, F. VESTA 3 for three-dimensional visualization of crystal, volumetric and morphology data. *Journal of applied crystallography* **2011**, *44* (6), 1272−1276.
(41) Hu, L.; Wang, J.; Wang, K.; Gu, Z.; Xi, Z.; Li, H.; Chen, F.; Wang, Y.; Li, Z.; Ma, C. A cost-effective, ionically conductive and compressible oxychloride solid-state electrolyte for stable all-solid-state lithium-based batteries. *Nat. Commun.* **2023**, *14* (1), 3807.
(42) Perdew, J. P.; Burke, K.; Ernzerhof, M. Generalized gradient approximation made simple. *Physical review letters* **1996**, *77* (18), 3865.
(43) Kresse, G.; Furthmüller, J. Efficient iterative schemes for ab initio total-energy calculations using a plane-wave basis set. *Phys. Rev. B* **1996**, *54* (16), 11169−11186.
(44) Kresse, G.; Furthmüller, J. Efficiency of ab-initio total energy calculations for metals and semiconductors using a plane-wave basis set. *Comput. Mater. Sci.* **1996**, *6* (1), 15−50.
(45) Monkhorst, H. J.; Pack, J. D. Special points for Brillouin-zone integrations. *Phys. Rev. B* **1976**, *13* (12), 5188.
(46) Blöchl, P. E. Projector augmented-wave method. *Phys. Rev. B* **1994**, *50* (24), 17953−17979.
(47) Heyd, J.; Scuseria, G. E.; Ernzerhof, M. Hybrid functionals based on a screened Coulomb potential. *J. Chem. Phys.* **2003**, *118* (18), 8207−8215.
(48) Henkelman, G.; Uberuaga, B. P.; Jónsson, H. A climbing image nudged elastic band method for finding saddle points and minimum energy paths. *J. Chem. Phys.* **2000**, *113* (22), 9901−9904.
(49) Hussain, F.; Zhu, J.; Xia, H.; Zhao, Y.; Xia, W. Theoretical Insights on the Comparison of Li-Ion Conductivity in Halide Superionic Conductors Li_3MCl_6, $Li_2M_{2/3}Cl_4$, and $LiMCl_4$ (M = Y, Sc, Al, and Sm). *J. Phys. Chem. C* **2022**, *126* (31), 13105−13113.
(50) Hussain, F.; Li, P.; Li, Z. Theoretical Insights into Li-Ion Transport in $LiTa_2PO_8$. *J. Phys. Chem. C* **2019**, *123* (32), 19282−19287.
(51) Hussain, F.; Yu, P.; Zhu, J.; Xia, H.; Zhao, Y.; Xia, W. Theoretical Prediction of Spinel $Na_2In_xSc_{0.666-x}Cl_4$ and Rock-Salt $Na_3In_{1-x}Sc_xCl_6$ Superionic Conductors for All-Solid-State Sodium-Ion Batteries. *Adv. Theory Simul.* **2023**, *6* (1), 2200569.

https://doi.org/10.1021/jacs.4c02170
J. Am. Chem. Soc. 2024, 146, 12681−12690